IET Image Processing

Research Article

IET Journals
The Institution of Engineering and Technology

Exact Legendre–Fourier moments in improved polar pixels configuration for image analysis

ISSN 1751-9659
Received on 16th May 2018
Revised 15th September 2018
Accepted on 22nd October 2018
doi: 10.1049/iet-ipr.2018.5489
www.ietdl.org

C. Camacho-Bello[1] ✉

[1]*Department of Computer Vision and Image Analysis, Universidad Politécnica de Tulancingo, Hidalgo, México*
✉ *E-mail: cesar.camacho@upt.edu.mx*

Abstract: This study presents the exact Legendre–Fourier moments and a novel arrangement of polar pixels that allows calculating orthogonal moments defined in a unit radius more accurately than traditional methods. This arrangement simplifies implementation and preserves the values of the pixels of the image during the calculation of the moments. Moreover, the exact Legendre–Fourier moments use the weighted substituted radial shifted Legendre polynomials as kernel, which has the ability to accurately calculate the circular moments. Finally, the author presents a comparative analysis of the reconstruction error with existing configurations and other families of circular moments. The results indicate that the mehod provides a significant advantage.

1 Introduction

Orthogonal moments are widely used in pattern recognition, image analysis, multimedia watermarking, and image retrieval [1]. The most significant property of orthogonal moments is their ability to characterise, evaluate, and manipulate information with minimum redundancy [2]. However, inaccurate computation of orthogonal moments may affect their capability. According to Liao and Pawlak [3], two types of errors occur in the computation of circular orthogonal moments: geometric errors and numerical integration errors.

To minimise geometric errors, Xin *et al.* [4] proposed a more accurate algorithm to compute circular orthogonal moments, where the original image was mapped to a polar pixel scheme using third-order bicubic interpolation introduced by Keys [5]. Even though interpolation errors are of secondary importance compared to discretisation errors, interpolation errors play a significant role in determining the accuracy of the algorithm. In addition, this algorithm is computationally expensive because the input image needs to be interpolated to a new location in the polar pixel configuration. Furthermore, this algorithm seeks new polar pixel configurations in order to streamline the computation of circular orthogonal moments with the aim to reduce reconstruction error and promote invariance. Singh and Walia [6] proposed an improved polar pixel configuration, which reduces the number of polar pixels and computational time by 27.3%. Likewise, Liu *et al.* [7] proposed an improved polar pixel scheme, which computes only one-sixteenth of the unit disk. Fig. 1 shows a comparison of the polar pixel configurations proposed by Xin *et al.* [4], Singh and Walia [6], and Liu *et al.* [7].

In order to minimise numerical integration errors, Xin *et al.* [4] solved the integral analytically using orthogonal polynomial coefficients. However, this approach results in numerical instability for higher order polynomials. Camacho-Bello *et al.* [8] used recurrence relations and numerical integration to reduce numerical integration errors and this approach was shown to be less accurate but more numerically stable for higher order polynomials. Sáez-Landete [9] recently showed that the configuration of Xin *et al.* [4] and the use of recurrence relations improved the reconstruction performance compared with the algorithm proposed by Upneja and Singh [10] for fast, accurate computations of circular moments.

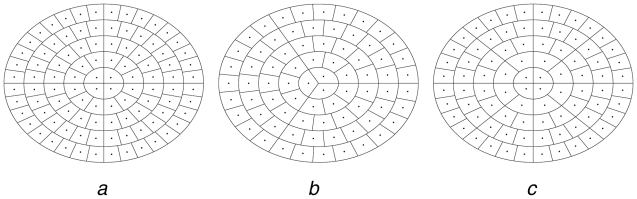

Fig. 1 *Polar pixel configurations proposed by* ***(a)*** Xin *et al.* [4], ***(b)*** Singh and Walia [6], ***(c)*** Liu *et al.* [7]

The polar pixel scheme proposed by Xin *et al.* [4] is widely used in the computation of circular orthogonal moments [8, 11, 12] as well as in applications such as shape feature extraction and description [13], speech content authentication [14], reconstruction of colour biomedical images [15], and colour image watermarking [16]. However, this polar pixel scheme is dependent on numerical interpolation, which repeats the information in some sectors. In addition, this scheme results in poor representation of the image in polar pixels, which in turn, affects the invariance of the moments to rotation and scale.

Hence, it is important to improve the manner in which the polar pixels are distributed in order to obtain a better description of the image, which will greatly facilitate basic and detailed image analyses. In basic image analysis, improving the polar pixel configuration enables the extraction of some interesting image features such as colour, sharp, and blur features whereas in detailed image analysis, improving the polar pixel configuration enables the extraction of visual information [17]. In addition, improved polar pixel configurations can be used in generalised sampling expansions such as the fractional Fourier transform [18]. Improving image reconstruction from circular orthogonal moments will be useful for image super-resolution reconstruction, which involves generating noise-free, blur-free, high-resolution images from noisy, blurry, low-resolution input images [19]. Furthermore, improved polar pixel configurations can enhance applications where orthogonal circular moments are used such as synthetic aperture radar image analysis [20, 21].

Owing to the importance of polar pixel configurations in image reconstruction, in this work, a novel polar pixel configuration is proposed based on concentric rings, where each ring is composed of irregular-sized pixels, which eliminates numerical interpolation, minimises information redundancy, improves rotation invariance and scale invariance, and enhance image description. Previous studies [22, 23] have also shown that Legendre polynomials, as kernel functions of orthogonal moments, perform exceptionally well for image reconstruction. Legendre polynomials are also used to compute fractional-order orthogonal moments [24] and moment invariants in the Radon space [25]. In addition, Legendre polynomials are used to compute Cartesian moments [26, 27]

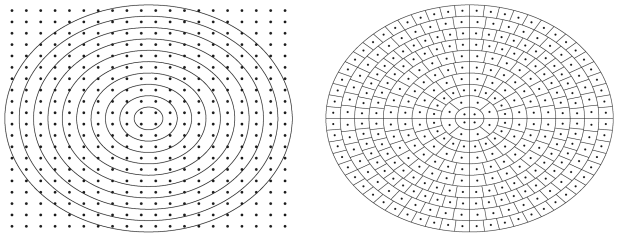

Fig. 2 *Example of the proposed configuration*
(a) Concentric rings in the distribution of pixels. ***(b)*** Proposed configuration of polar pixels

for $u = 0$ **to** $N/2 - 1$ **do**
  $r_u \leftarrow \frac{2u}{N}$
  $V_u \leftarrow$ *polar_pixels(u)*
  for $v = 0$ **to** $V_u - 1$ **do**
    $\theta_{u,v} \leftarrow \pi\,(2v + 1)\,/V_u$
  end for
end for

Fig. 3 *Algorithm 1: Polar pixels coordinates*

Configuration	*polar_pixels(u)*
Xin et al. [4]	$V_u \leftarrow 4\,(2u + 1)$
Singh and Walia [6]	$V_u \leftarrow 3\,(2u + 1)$

Liu et al. [7]	**if** $u = 0$ **then**
	$V_0 \leftarrow 4$
	else
	$V_u \leftarrow 8u$
	end if

Proposed configuration	$V_u \leftarrow 0$
	for $i = 0$ **to** $N - 1$ **do**
	for $j = 0$ **to** $M - 1$ **do**
	if $\frac{2(u-1)}{N} < r_{ij} < \frac{2u}{N}$ **then**
	$V_u \leftarrow V_u + 1$
	end if
	end for
	end for

Fig. 4 *Different configurations for V_u*

because these polynomials can compute the integral of the kernel functions with high accuracy. Hence, in this work, the Legendre polynomials are modified as weighted and substituted radial shifted Legendre polynomials in order to compute orthogonal moments in the new polar pixel configuration with high accuracy. Precise computation of the kernel functions guarantees that the image descriptors are linearly independent with minimal redundant information. The proposed polar pixel configuration is also compared with those of other researchers and the configurations are assessed in terms of the reconstruction error, rotation invariance, scale invariance, and their capability in reconstructing images corrupted with Gaussian noise. It is believed that the findings in this paper will be useful to those in the academia and industry involved in advancing the mathematical concepts of image reconstruction.

2 Proposed configuration

The image $\hat{f}(r_u, \theta_{uv})$ in polar pixels, defined by Xin *et al.* [4] as a set of concentric sectors Ω_{uv} that are non-overlapping, forms different configurations, as shown in Fig. 1. In this paper, the author proposes a novel arrangement of polar pixels that is based on placing a polar pixel at each point or pixel of the image in order to discard the numerical interpolation step required in the above configurations. To achieve this, the author considers an image $f(r_{ij}, \theta_{ij})$ with spatial dimensions $N \times M$, where the polar coordinates are expressed by

$$r_{ij} = \sqrt{x_i^2 + y_j^2}, \quad r_{i,j} \leq 1 \tag{1}$$

$$\theta_{ij} = \arctan\left(\frac{y_j}{x_i}\right) \tag{2}$$

and are transformed by

$$x_i = \frac{2i + 1 - N}{N}, \quad y_j = \frac{2j + 1 - M}{M}, \tag{3}$$

where $i = 0, \ldots, N - 1$, and $j = 0, \ldots, M - 1$. Thus, we build the polar pixels arrangement from the dimensions of the image $f(r_{ij}, \theta_{ij})$. We start by dividing the unit radius in $N/2$ concentric rings, which are separated at $\{(2u/N),\ u = 1, \ldots, N/2\}$, as shown in Fig. 2*a*. The pixels that are in the range

$$\frac{2(u-1)}{N} < r_{ij} < \frac{2u}{N}, \tag{4}$$

form the sectors or polar pixels of each concentric ring u. Further, the coordinates of the arrangement of polar pixels are given in Algorithm 1 (Fig. 3), where V_u is the total number of pixels that are in the concentric ring u.

The function *polar_pixels (u)* of the proposed configuration and different configurations are given in Fig. 4. The proposed configuration ensures that all pixels in the image are contained in a polar pixel. For any image of size $N \times N$, the values V_u can be calculated by the restriction of (4). Fig. 2*b* shows the proposed arrangement of polar pixels for an image of 20×20 pixels. The size of the polar pixels varies for each ring. In Fig. 2*b*, the size of the polar pixels is given by

$$r_u \frac{2\pi}{V_u} = \langle 0.16, 0.16, 0.09, 0.12, 0.11, 0.12, 0.10, 0.10, 0.12, 0.10 \rangle \tag{5}$$

where

$$r_u = \langle 0.1, 0.2, 0.3, 0.4, 0.5, 0.6, 0.7, 0.8, 0.9, 1.0 \rangle$$
$$V_u = \langle 4, 8, 20, 20, 28, 32, 44, 52, 48, 60 \rangle$$

Each ring of Fig. 2*a* considers a certain number of points or pixels. In the example presented, rings 3 and 4 both have 20 points, and their size is 0.09 and 0.12, respectively. Xin *et al.* [4] recommend that all polar pixels have the same size. However, it is not necessary that the polar pixels have the same size as long as all the image information is considered. In the proposed configuration, the number of polar pixels varies for each concentric ring, this is in order to assign each pixel of the image within the unit circle. Note that the concentric rings shown in Fig. 2*a* match the polar pixels of

Table 1 6×6 synthetic image

123	45	67	32	21	134
221	234	29	63	65	89
129	212	234	73	98	141
56	91	83	69	84	198
73	0	58	45	14	189
28	255	245	64	7	154

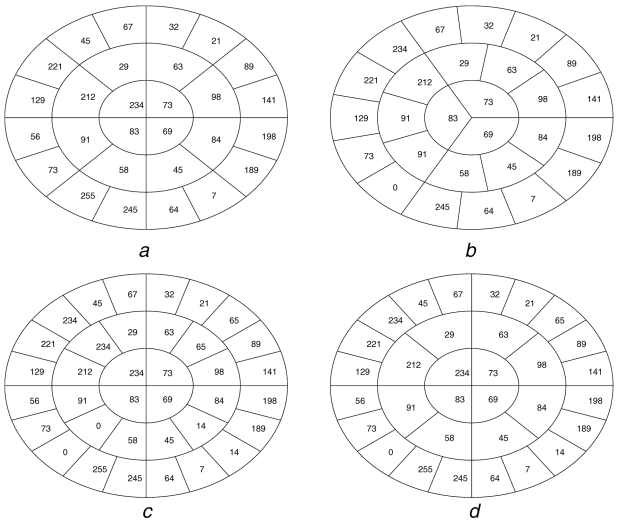

Fig. 5 *Polar pixel arrangement of the synthetic image*
(a) The configuration of Liu *et al.* [7], ***(b)*** The configuration of Singh and Walia [6], ***(c)*** The configuration of Xin *et al.* [4], ***(d)*** Proposed configuration

Fig. 2*b*. Accordingly, we can take numerical values of the image for each image sector in polar pixels.

A synthetic image shown in Table 1 is used to demonstrate that the proposed configuration considers all pixels of the image are inside the unit circle. In addition, it is used to represent the arrangement of polar pixels in different configurations.

Fig. 5 shows the synthetic image with the polar pixel arrangement of Liu *et al.* [7], Singh and Walia [6], Xin *et al.* [4] and the proposed configuration. In the representation of different configurations, the values of the corners 123, 134, 28, and 154 are outside of the unit circle. Note that the Liu *et al.* [7] configuration, loses the values 234, 65, 0, and 14 unlike Xin *et al.* [4] configuration, where the values 234, 65, 0 and 14 repeats. On the other hand, the Singh and Walia [6] configuration loses the values 234, 65, 14, 56, 255, 45 and repeats 91. The proposed configuration is the only one that considers all the pixels within the unit circle in its representation. Moreover, the results of Section 5 show that the proposed configuration with different polar pixel sizes improves upon configurations that have similar sizes.

On the other hand, the computation time of the polar pixel configuration and the interpolation of the methods of Liu *et al.* [7], Singh and Walia [6], Xin *et al.* [4], and the proposed configuration are shown in Fig. 6. The algorithms were implemented in MATLAB on a PC Intel® Core™ i7-6500U 2.50 Hz, 8 GB RAM. Note that the computation time of the proposed configuration is better than the different configurations because it does not perform an interpolation with the original image.

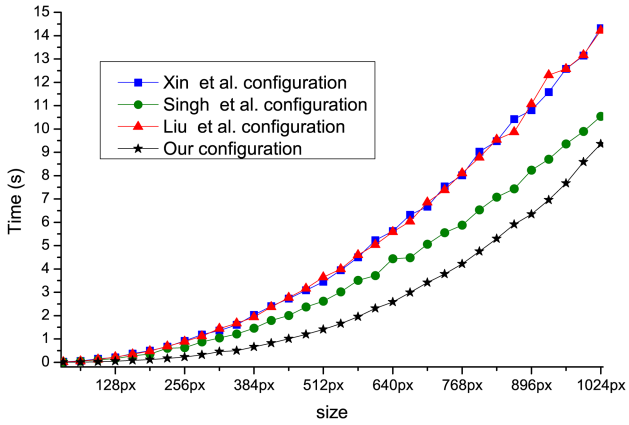

Fig. 6 *Computational times of different configurations of polar pixels*

3 Weighted substituted radial shifted Legendre polynomials (WSRSLPs)

In this section, the author proposes a recurrence relation for the WSRSLPs and a relation to calculate the kernel integral in an exact way. The deduction comes from the Legendre polynomials, which are given as follows:

$$nL_n(r) = (2n-1)rL_{n-1}(r) - (n-1)L_{n-2}(r), \tag{6}$$

with $L_0(r) = 1$, $L_1(r) = r$. An important property of the Legendre polynomials $L_n(r)$ is that they are orthogonal over $[-1, 1]$, with

$$\int_{-1}^{1} L_n(r)L_m(r)\mathrm{d}r = \frac{2}{2n+1}\delta_{nm}. \tag{7}$$

Another important property is the integration of Legendre polynomials, which is given by

$$\int L_n(r)\mathrm{d}r = \frac{L_{n+1}(r) - L_{n-1}(r)}{2n+1} \tag{8}$$

In order for the Legendre polynomials to be used as kernel of circular moments, they must be defined inside of the unit circle where the orthogonality interval is defined in [0, 1].

With the help of Legendre polynomials, we can derive WSRSLPs $\hat{L}_n(r)$, which can be obtained by the following relationships:

$$\hat{L}_n(r) = \sqrt{2(2n+1)}L_n\left(2r^2 - 1\right) \tag{9}$$

In the same way as the Legendre polynomials, we can obtain the orthogonality condition, the recurrence relation and the integration of WSRSLPs.

Theorem 1: Weighted substituted radial shifted Legendre polynomials are orthogonal over in the interval [0, 1] *with* the *weighted function* $\sqrt{2(2n+1)}$

$$\int_0^1 \hat{L}_n(r)\hat{L}_m(r)r\,\mathrm{d}r = \delta_{nm} \tag{10}$$

Proof: By substituting $L_n(2r^2-1) = \hat{L}_n(r)/\sqrt{2(2n+1)}$ to (7), we have

$$\begin{aligned}\int_{-1}^1 L_n(r)L_n(r)\mathrm{d}r &= \int_0^1 L_n(2r^2-1)L_n(2r^2-1)4r\,\mathrm{d}r \\ &= \int_0^1 \frac{\hat{L}_n(r)\hat{L}_m(r)4r}{2(2n+1)}\mathrm{d}r \\ &= \frac{2}{2n+1}\int_0^1 \hat{L}_n(r)\hat{L}_m(r)r\,\mathrm{d}r \\ &= \frac{2}{2n+1}\delta_{nm}\end{aligned}$$

□

Lemma 2: The recurrence relation of the weighted substituted radial shifted Legendre polynomials is given by

$$a_n\hat{L}_n(r) = (2r^2-1)\hat{L}_{n-1}(r) - a_{n-1}\hat{L}_{n-2}(r) \tag{11}$$

where

$$a_n = \frac{n}{\sqrt{4n^2-1}} \tag{12}$$

For the initial numerical values, the zeroth and first normalised orders are, respectively, given by

$$\begin{aligned}\hat{L}_0(r) &= \sqrt{2} \\ \hat{L}_1(r) &= \sqrt{6}(2r^2-1)\end{aligned}$$

Proof: By substituting $L_n(2r^2-1) = \hat{L}_n(r)/\sqrt{2(2n+1)}$ to (6), we have

$$\begin{aligned}nL_n(2r^2-1) &= (2n-1)(2r^2-1)L_{n-1}(2r^2-1) \\ &\quad -(n-1)L_{n-2}(2r^2-1) \\ \frac{n\hat{L}_n(r)}{\sqrt{2(2n+1)}} &= \frac{2n-1}{\sqrt{2(2n-1)}}(2r^2-1)\hat{L}_{n-1}(r) \\ &\quad -\frac{(n-1)\hat{L}_{n-2}(r)}{\sqrt{2(2n-3)}} \\ \frac{n\hat{L}_n(r)}{\sqrt{(2n+1)(2n-1)}} &= (2r^2-1)\hat{L}_{n-1}(r) - \frac{(n-1)\hat{L}_{n-2}(r)}{\sqrt{(2n-1)(2n-3)}} \\ \frac{n\hat{L}_n(r)}{\sqrt{4n^2-1}} &= (2r^2-1)\hat{L}_{n-1}(r) - \frac{(n-1)\hat{L}_{n-2}(r)}{\sqrt{4(n-1)^2-1}}\end{aligned}$$

□

Lemma 3: The integration of the weighted substituted radial shifted Legendre polynomials can be given as follows:

$$\int \hat{L}_n(r)r\,\mathrm{d}r = \frac{1}{2\sqrt{4n+2}}\left[\frac{\hat{L}_{n+1}(r)}{\sqrt{4n+6}} - \frac{\hat{L}_{n-1}(r)}{\sqrt{4n-2}}\right] \tag{13}$$

Proof: By substituting $L_n(2r^2-1) = \hat{L}_n(r)/\sqrt{2(2n+1)}$ to (8), we have

$$\begin{aligned}\int L_n(2r^2-1)4r\,\mathrm{d}r &= \frac{L_{n+1}(2r^2-1) - L_{n-1}(2r^2-1)}{2n+1} \\ \int \frac{\hat{L}_n(r)4r}{\sqrt{2(2n+1)}}\mathrm{d}r &= \frac{1}{2n+1}\left[\frac{\hat{L}_{n+1}(r)}{\sqrt{4n+6}} - \frac{\hat{L}_{n-1}(r)}{\sqrt{4n-2}}\right] \\ \int \hat{L}_n(r)r &= \frac{1}{2\sqrt{4n+2}}\left[\frac{\hat{L}_{n+1}(r)}{\sqrt{4n+6}} - \frac{\hat{L}_{n-1}(r)}{\sqrt{4n-2}}\right]\end{aligned}$$

□

4 Exact Legendre–Fourier moments

The arrangement of polar pixels is used for the fast and high-precision calculation of the orthogonal moments defined in the unit disk [8]. In this paper, WSRSLPs as the kernel of the circular moments to implement the proposed configuration were used, along with the ability to calculate the integral kernel accurately. The general expression for exact Legendre–Fourier moments (ELFMs) of order n and repetition m, for a given image function $f(r,\theta)$ in polar coordinates, is given by

$$\phi_{n,m} = \int_0^{2\pi}\int_0^1 f(r,\theta)P_{nm}(r,\theta)r\,\mathrm{d}r\,\mathrm{d}\theta, \tag{14}$$

where $P_{nm}(r,\theta)$ is the kernel function, which consists of two separable functions sets: WSRSLPs $\hat{L}_n(r)$ and the exponential Fourier factor $\exp(jm\theta)$.

The calculation of the ELFMs in the new arrangement of polar pixels is performed by the summation of all sectors Ω_{uv}. Therefore, (14) can be rewritten as

$$\hat{\phi}_{nm} = \frac{1}{2\pi}\sum_{u=1}^{U}\sum_{v=1}^{V_u}\hat{f}(r_u,\theta_{uv})\omega_{nm}(r_u,\theta_{uv}) \tag{15}$$

where $\hat{f}(r_u,\theta_{uv})$ is an approximation of the function $f(r_{i,j},\theta_{i,j})$ defined over a set of concentric sectors Ω_{uv} and the factor $\omega_{nm}(r_u,\theta_{uv})$ is given by

$$\begin{aligned}\omega_{nm}(r_u,\theta_{uv}) &= \int\int_{\Omega_{uv}}\hat{L}_n(r)\exp(jm\theta)r\,\mathrm{d}r\,\mathrm{d}\theta \\ &= \int_{r_{uv}^{(s)}}^{r_{uv}^{(e)}}\hat{L}_n(r)r\,\mathrm{d}r\int_{\theta_{uv}^{(s)}}^{\theta_{uv}^{(e)}}\exp(jm\theta)\mathrm{d}\theta \\ &= I_1\times I_2\end{aligned} \tag{16}$$

where $(r_u^{(s)},\theta_{uv}^{(e)})$, $(r_u^{(s)},\theta_{uv}^{(s)})$, $(r_u^{(e)},\theta_{uv}^{(e)})$ and $(r_u^{(e)},\theta_{uv}^{(s)})$ denote the starting and ending points of the sector Ω_{uv}, where (r_u,θ_{uv}) represent the radius and angle, respectively, of each sector Ω_{uv}. The calculation for the integral of the WSRSLPs can be analytically calculated as

$$\begin{aligned}I_1 &= \frac{\left[\hat{L}_{n+1}(r_u^{(e)}) - \hat{L}_{n+1}(r_u^{(s)})\right]}{2\sqrt{(4n+6)(4n+2)}} \\ &\quad -\frac{\left[\hat{L}_{n-1}(r_u^{(e)}) - \hat{L}_{n-1}(r_u^{(s)})\right]}{2\sqrt{(4n-2)(4n+2)}},\end{aligned} \tag{17}$$

and the integral of the complex Fourier component is given by

$$I_2 = \begin{cases}\dfrac{j}{m}\left[\exp(-jm\theta_{uv}^{(e)}) - \exp(-jm\theta_{uv}^{(s)})\right], & m\neq 0 \\ \theta_{uv}^{(e)} - \theta_{uv}^{(s)}, & m = 0\end{cases}. \tag{18}$$

5 Experiments and results

In this section, the configurations of Fig. 1 from four different perspectives, representation and reconstruction of a synthetic image, a 512×512 pixels image reconstruction, noisy image

Fig. 7 *15 standard test images of size* 512×512 *pixels*

reconstruction, and invariance to rotation and scale were compared. Furthermore, the exact Legendre–Fourier moments with other different families of circular moments all calculated in the framework of polar pixels with the proposed configuration were also compared. The test images are shown in Fig. 7.

5.1 Improvement of image reconstruction

Image reconstruction can help determine how well an image may be characterised by a finite set of its moments. According to orthogonal theories, an original image $f(i, j)$ can be reconstructed by an infinite number of ELFMs. The reconstructed discrete distribution of the image is given by

$$\tilde{f}(i,j) = \sum_{n=0}^{L} \sum_{m=-L}^{L} \hat{\phi}_{nm} L_n(r_{ij}) \exp(-jm\theta_{ij}) \tag{19}$$

where $\tilde{f}(i, j)$ is the reconstructed version of $f(i, j)$, and L is the maximum order of ELFMs used in the reconstruction of the image. Fig. 8 shows image reconstruction with the proposed configuration and other configurations.

NIRE is defined as the normalised mean square error between the input image $f(i, j)$ and its reconstruction $\tilde{f}(i, j)$, and it is used for the performance analysis of orthogonal moments. Its discrete form is

$$\text{NIRE} = \frac{\sum_{i=0}^{N-1} \sum_{j=0}^{M-1} \left[\tilde{f}(i,j) - f(i,j)\right]^2}{\sum_{i=0}^{N-1} \sum_{j=0}^{M-1} f^2(i,j)}, \tag{20}$$

and the results are shown in Fig. 9. The improvements in Fig. 8 are not very noticeable at the first glance; however, NIRE demonstrates the superiority of the proposed configuration.

5.2 Noisy image reconstruction

High resistance to noise is a property of low-order orthogonal moments. The different configurations of polar pixels with the peak signal-to-noise ratio (PSNR) were compared and the performance of PSNR for image reconstruction of images was degraded by Gaussian noise. PSNR is the ratio between the maximum power of a signal and the power of the signal noise, and it is usually expressed in decibels with the logarithmic scale. It can be calculated as

$$\text{PSNR} = 10 \log_{10}\left(\frac{255^2}{\text{MSE}}\right) \tag{21}$$

where *MSE* is the mean square error defined by

$$\text{MSE} = \frac{1}{N \times M} \sum_{i=0}^{N-1} \sum_{j=0}^{M-1} \left[\tilde{f}(i,j) - f(i,j)\right]^2. \tag{22}$$

Fig. 10 shows the test images degraded by noise. Also, PSNR of the test images with noise are presented in Fig. 11. As in the case

Fig. 8 *Test images reconstructed with ELFMs and* $L = 100$ *for different configurations of polar pixels*

of NIRE, the proposed configuration provides better results in resisting the Gaussian noise than other polar pixel configuration.

5.3 Improvement of rotation and scale invariance

One of the most important properties of circular moments is the invariant representation of the scaled and rotated object. If a distorted image $f(r/k, \theta - \gamma)$ is rotated by γ degrees and scaled by a factor k, all ELFMs of the resulting image, $\hat{\phi}_{nm}^{(\gamma,k)}$, are related with the ELFMs of the original image by

$$\hat{\phi}_{nm}^{(\gamma,k)} = \hat{\phi}_{nm} \mathrm{e}^{-\mathrm{i}m\gamma}. \tag{23}$$

Therefore, modulus ELFMs

$$\left|\hat{\phi}_{nm}^{(\gamma,k)}\right| = \left|\hat{\phi}_{nm}\right|, \tag{24}$$

is invariant to scale and rotation. In the accurate calculation, it is not required that (24) be normalised by the scaling factor k because the unit circle is independent of the image. All scaled images $(N \times N)k$ can be defined within the unit circle regardless of their size, therefore the moment values are the same.

A measure to facilitate the comparison among different orthogonal moment calculations is by normalised mean squared error (NMSE) which is given as follows:

$$\mathrm{NMSE}\left(\left|\hat{\phi}_{nm}\right|, \left|\hat{\phi}_{nm}^{(\gamma,k)}\right|\right) = \frac{1}{L^2} \sum_{n=1}^{L} \sum_{m=1}^{L} \frac{\left(\left|\hat{\phi}_{nm}^{(\gamma,k)}\right| - \left|\hat{\phi}_{nm}\right|\right)^2}{\left|\hat{\phi}_{nm}\right|^2}, \tag{25}$$

where L^2 is the number of ELFMs involved in the evaluation. In Table 2, the NMSE with rotation angles of 55° and −135°, and with scale changes of $k = 0.75$ and $k = 1.25$ are shown. For each rotation angle and scale, the first 100 ELFMs ($L = 10$) are calculated. It is clear that the proposed method greatly surpasses different configurations in terms of its invariance to rotation and scale.

5.4 Comparisons with other families of circular moments

Recent work has introduced different families of circular moments such as Zernike moments (ZMs, [2]), weighted radial shifted Legendre moments [23], Pseudo-Zernike moments [28], Pseudo-Jacobi–Fourier moments [29], Chebyshev–Fourier moments [30], orthogonal Fourier–Mellin moments [31], radial-harmonic-Fourier moments [32], and Bessel–Fourier moments [33] with the aim of finding the circular moments that best represent an image. However, they are calculated with zero-order approximation (ZOA) affecting their ability description. Moreover, arrangement of polar pixels has proved fast and high-precision compared to ZOA [8]. In this section, ELFMs are compared with different families of circular moments in terms of image reconstruction and NIRE; they all calculated with the proposed configuration of polar pixels. The results are shown in Fig. 12.

6 Conclusions

In this paper, a novel approach for computation of ELFMs is proposed. Exact calculation of the integral of WSRSLPs from (17) removes numerical approximation errors; this is seen in Section 5.4, where the ELFMs are compared with other families of circular moments using numerical integration. Moreover, a novel configuration for the distribution of polar pixels is presented, which facilitates implementation, is efficient in terms of image reconstruction, and is resistant to noise. Furthermore, the actual numerical values of the original image in the proposed configuration are used, unlike configurations of Xin *et al.* [4], Singh and Walia [6], and Liu *et al.* [7], which required numerical interpolation to obtain the values of each polar pixel. The proposed configuration demonstrates that it is not necessary for polar pixels to have the same size as stated by Xin *et al.* [4]. Also, this

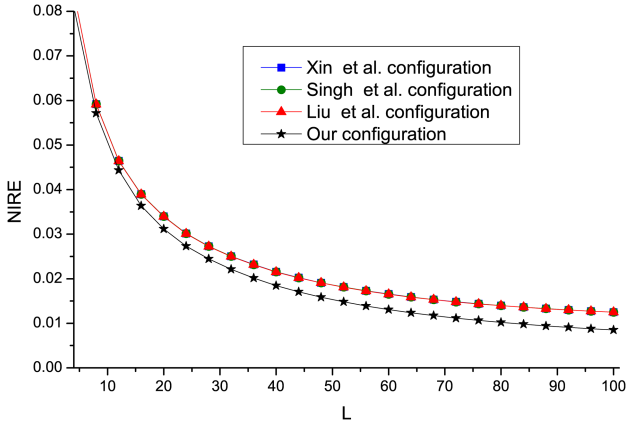

Fig. 9 *NIRE average of the test images for different configurations of polar pixels*

Fig. 10 *15 standard test images corrupted by additive Gaussian noise of zero mean and* $\sigma^2 = 0.1$

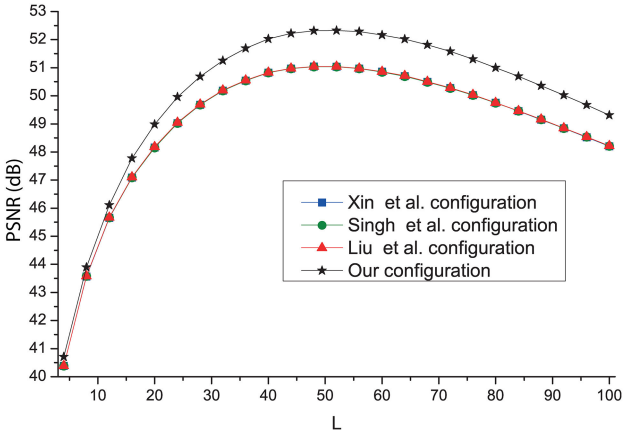

Fig. 11 *dB average of the test images for different configurations of polar pixels*

configuration can be implemented on other families of circular moments, such as radial moments [34], quaternion colour moments in polar pixels [35], moment invariants in the Radon space [25], and fractional-order orthogonal moments [24].

Table 2 Test of rotation and scale invariance with 15 standard images degraded by scale and angle changes

Image name	Xin *et al.*				Singh and Walia				Liu *et al.*				Our configuration			
	k	k	γ	γ	k	k	γ	γ	k	k	γ	γ	k	k	γ	γ
	0.75	1.25	55°	−135°	0.75	1.25	55°	−135°	0.75	1.25	55°	−135°	0.75	1.25	55°	−135°
woman darkhair	0.0074	0.0022	0.0993	0.1792	0.0321	0.0449	1.2726	1.2391	0.0050	0.0028	0.0953	0.1590	0.0040	0.0004	0.0197	0.0198
woman blonde	0.0031	0.0017	0.0386	0.1300	0.0036	0.0023	0.0529	0.1263	0.0030	0.0015	0.0391	0.1329	0.0001	0.0001	0.0002	0.0004
house	0.0114	0.0047	0.0556	0.3909	0.0142	0.0052	0.0517	0.4190	0.0126	0.0045	0.0560	0.3790	0.0003	0.0001	0.0010	0.0007
lake	0.0058	0.0025	0.0379	0.1519	0.0076	0.0029	0.0399	0.1502	0.0057	0.0036	0.0402	0.1239	0.0076	0.0002	0.0023	0.0027
jetplane	0.0130	0.0043	0.1394	0.2579	0.0115	0.0041	0.1300	0.2563	0.0104	0.0045	0.1283	0.2613	0.0002	0.0001	0.0008	0.0010
livingroom	0.0153	0.0119	0.2025	0.2542	0.0138	0.0192	1.1752	1.0747	0.0236	0.0157	0.8566	0.8859	0.0009	0.0003	0.0034	0.0022
walkbridge	0.0293	0.0288	0.0800	0.8395	0.0477	0.0112	0.1125	1.1018	0.0234	0.0173	0.0554	0.6986	0.0010	0.0002	0.0020	0.0010
Lena	0.0042	0.0020	0.1908	0.1631	0.0060	0.0026	0.1863	0.1577	0.0045	0.0017	0.1785	0.1593	0.0008	0.0002	0.0004	0.0005
cameraman	0.0088	0.0083	0.0368	1.2248	0.0061	0.0118	0.0774	1.8848	0.0047	0.0204	0.0559	2.1339	0.0016	0.0004	0.0069	0.0053
Barbara	0.0138	0.0098	0.0438	0.0660	0.0162	0.0126	0.0429	0.0821	0.0176	0.0108	0.0473	0.0784	0.0070	0.0011	0.0062	0.0038
peppers	0.0365	0.0506	0.3182	2.4258	0.0303	0.0074	0.1107	0.6718	0.2043	0.0880	0.6213	6.0141	0.0025	0.0006	0.0024	0.0022
Goldhill	0.0083	0.0313	0.1223	0.6511	0.0135	0.0102	0.1081	0.2891	0.0131	0.0092	0.0922	0.3411	0.0012	0.0002	0.0020	0.0014
mandril	0.3184	0.0994	3.4033	4.7199	0.0700	0.0308	1.2345	2.8218	0.0958	0.0253	1.7473	2.4138	0.0051	0.0008	0.0120	0.0092
pirate	0.0151	0.0101	0.0357	0.4443	0.0131	0.0062	0.0249	0.3261	0.0108	0.0111	0.0340	0.4734	0.0055	0.0002	0.0130	0.0038
boat	0.0208	0.0022	0.1025	0.2636	0.0144	0.0052	0.0864	0.2012	0.0158	0.0030	0.0997	0.2161	0.0003	0.0002	0.0006	0.0005
average	0.0341	0.0180	0.3271	0.8108	0.0200	0.0118	0.0118	0.7201	0.0300	0.0146	0.2765	0.9647	0.0025	0.0003	0.0049	0.0036

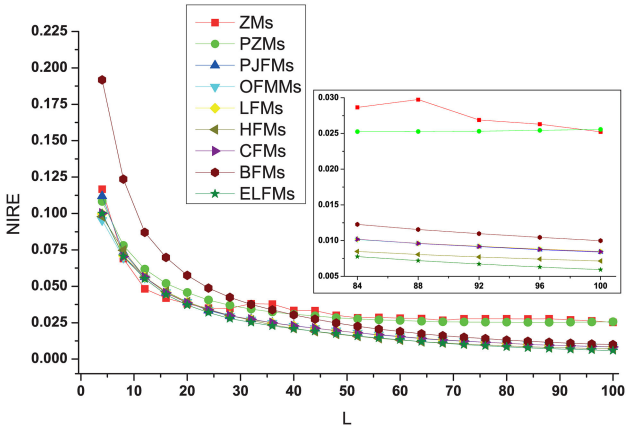

Fig. 12 *NIRE average of the test images for different families of circular moments with our configuration of polar pixels*

7 References

[1] Papakostas, G.A.: 'Over 50 years of image moments and moment invariants', in Papakostas, G.A. (Ed.): '*Moments moment invariants-theor app*' (Science Gate Publishing, Xanthi, Greece, 2014), pp. 3–32

[2] Teague, M.R.: 'Image analysis via the general theory of moments', *JOSA*, 1980, **70**, (8), pp. 920–930

[3] Liao, S.X., Pawlak, M.: 'On the accuracy of Zernike moments for image analysis', *IEEE Trans. Pattern Anal. Mach. Intell.*, 1998, **20**, (12), pp. 1358–1364

[4] Xin, Y., Pawlak, M., Liao, S.: 'Accurate computation of Zernike moments in polar coordinates', *IEEE Trans. Image Process.*, 2007, **16**, (2), pp. 581–587

[5] Keys, R.: 'Cubic convolution interpolation for digital image processing', *IEEE Trans. Acoust. Speech Signal Process.*, 1981, **29**, (6), pp. 1153–1160

[6] Singh, C., Walia, E.: 'Computation of Zernike moments in improved polar configuration', *IET Image Process.*, 2009, **3**, (4), pp. 217–227

[7] Liu, C., Huang, X.-H., Wang, M.: 'Fast computation of Zernike moments in polar coordinates', *IET Image Process.*, 2012, **6**, (7), pp. 996–1004

[8] Camacho-Bello, C., Toxqui-Quitl, C., Padilla-Vivanco, A., *et al.*: 'High-precision and fast computation of Jacobi–Fourier moments for image description', *JOSA A*, 2014, **31**, (1), pp. 124–134

[9] Sáez-Landete, J.: 'Comments on fast computation of Jacobi-Fourier moments for invariant image recognition', *Pattern Recognit.*, 2017, **67**, pp. 16–22

[10] Upneja, R., Singh, C.: 'Fast computation of Jacobi-Fourier moments for invariant image recognition', *Pattern Recognit.*, 2015, **48**, (5), pp. 1836–1843

[11] Hosny, K.M., Darwish, M.M.: 'New set of quaternion moments for color images representation and recognition', *J. Math. Imaging Vis.*, 2018, **60**, (5), pp. 717–736

[12] Hosny, K.M., Darwish, M.M.: 'Highly accurate and numerically stable higher order QPCET moments for color image representation', *Pattern Recognit. Lett.*, 2017, **97**, pp. 29–36

[13] Ma, Z.M., Zhang, G., Yan, L.: 'Shape feature descriptor using modified Zernike moments', *Pattern Anal. Appl.*, 2011, **14**, (1), pp. 9–22

[14] Liu, Z., Wang, H.: 'A novel speech content authentication algorithm based on Bessel–Fourier moments', *Digit. Signal Process.*, 2014, **24**, pp. 197–208

[15] Camacho-Bello, C., Padilla-Vivanco, A., Toxqui-Quitl, C., *et al.*: 'Reconstruction of color biomedical images by means of quaternion generic Jacobi–Fourier moments in the framework of polar pixels', *J.Med. Imag.*, 2016, **3**, (1), p. 014004

[16] Hosny, K.M., Darwish, M.M.: 'Robust color image watermarking using invariant quaternion Legendre–Fourier moments', *Multimedia Tools Appl.*, 2018, **77**, (19), pp. 24727–24750

[17] Lahrache, S., El Ouazzani, R., El Qadi, A.: 'Rules of photography for image memorability analysis', *IET Image Process.*, 2018, **12**, (7), pp. 1228–1236

[18] Wei, D., Li, Y.M.: 'Generalized sampling expansions with multiple sampling rates for lowpass and bandpass signals in the fractional Fourier transform domain', *IEEE Trans. Signal Process.*, 2016, **64**, (18), pp. 4861–4874

[19] Wei, D.: 'Image super-resolution reconstruction using the high-order derivative interpolation associated with fractional filter functions', *IET Signal Process.*, 2016, **10**, (9), pp. 1052–1061

[20] Ji, J.: 'Robust approach to independent component analysis for SAR image analysis', *IET Image Process.*, 2012, **6**, (3), pp. 284–291

[21] Bolourchi, P., Demirel, H., Uysal, S.: 'Target recognition in SAR images using radial Chebyshev moments', *Signal. Image. Video. Process.*, 2017, **11**, (6), pp. 1033–1040

[22] Camacho-Bello, C., Toxqui-Quitl, C., Padilla-Vivanco, A.: 'Generic orthogonal moments and applications', in Papakostas, G.A. (Ed.): '*Moments moment invariants-theor app*' (Science Gate Publishing, Xanthi, Greece, 2014), pp. 175–204

[23] Xiao, B., Wang, G.-Y., Li, W.-S.: 'Radial shifted Legendre moments for image analysis and invariant image recognition', *Image Vis. Comput.*, 2014, **32**, (12), pp. 994–1006

[24] Xiao, B., Li, L., Li, Y., *et al.*: 'Image analysis by fractional-order orthogonal moments', *Inf. Sci.*, 2017, **382–383**, pp. 135–149

[25] Xiao, B., Cui, J.-T., Qin, H.-X., *et al.*: 'Moments and moment invariants in the radon space', *Pattern Recognit.*, 2015, **48**, (9), pp. 2772–2784

[26] Hosny, K.M.: 'Exact Legendre moment computation for gray level images', *Pattern Recognit.*, 2007, **40**, (12), pp. 3597–3605

[27] Papakostas, G.A., Karakasis, E.G., Koulouriotis, D.E.: 'Accurate and speedy computation of image Legendre moments for computer vision applications', *Image Vis. Comput.*, 2010, **28**, (3), pp. 414–423

[28] Xia, T., Zhu, H., Shu, H., *et al.*: 'Image description with generalized pseudo-Zernike moments', *JOSA A*, 2007, **24**, (1), pp. 50–59

[29] Amu, G., Hasi, S., Yang, X., *et al.*: 'Image analysis by pseudo-Jacobi (p = 4, q = 3)–Fourier moments', *Appl. Opt.*, 2004, **43**, (10), pp. 2093–2101

[30] Ping, Z.L., Wu, R.G., Sheng, Y.L.: 'Image description with Chebyshev–Fourier moments', *JOSA A*, 2002, **19**, (9), pp. 1748–1754

[31] Sheng, Y., Shen, L.: 'Orthogonal Fourier–Mellin moments for invariant pattern recognition', *JOSA A*, 1994, **11**, (6), pp. 1748–1757

[32] Ren, H., Ping, Z., Bo, W., *et al.*: 'Multidistortion-invariant image recognition with radial harmonic Fourier moments', *JOSA A*, 2003, **20**, (4), pp. 631–637

[33] Xiao, B., Ma, J.-F., Wang, X.: 'Image analysis by Bessel–Fourier moments', *Pattern Recognit.*, 2010, **43**, (8), pp. 2620–2629

[34] Mukundan, R.: 'Radial Tchebichef invariants for pattern recognition'. In Proc. TENCON 2005 - IEEE Region 10 Conf., Melbourne, Australia, November 2005, pp. 1–6

[35] Camacho-Bello, C., Báez-Rojas, J.J., Toxqui-Quitl, C., *et al.*: 'Color image reconstruction using quaternion Legendre-Fourier moments in polar pixels'. Proc. 2014 Int. Conf. Mechatronics, Electronics and Automotive Engineering (ICMEAE), Cuernavaca, Mexico, 2014, pp. 3–8